

Optical Engineering

OpticalEngineering.SPIEDigitalLibrary.org

Traceability of form measurements of freeform surfaces: metrological reference surfaces

Ines Fortmeier
Michael Schulz
Rudolf Meeß

Traceability of form measurements of freeform surfaces: metrological reference surfaces

Ines Fortmeier,* Michael Schulz, and Rudolf Meeß

Physikalisch–Technische Bundesanstalt, Bundesallee 100, 38116 Braunschweig, Germany

Abstract. Due to the complexity of measurement systems for asphere and freeform surfaces, well-known artifacts are required to characterize the accuracy of the results of their form measurements. We present advancements in manufacturing and characterization of metrological multispherical freeform artifacts. The strong cooperation between the manufacturing and measurement units of Physikalisch–Technische Bundesanstalt (PTB) allows the form of the artifacts to be manufactured very accurately and the root-mean-square deviation from the desired design form to be improved by a factor of >20 compared to former results (e.g., from a value >500 nm to about 20 nm). Furthermore, a nickel/phosphorous coating is added to the copper surface, resulting in greater hardness and allowing the coated surface to be used as a reference for low-force tactile measurement systems. Four Gaussian peak fiducial marker structures are added to the design to improve the evaluation of comparison measurements. In addition to characterizing the radii in the spherical segments using PTB's radius measurement bench, we also characterize the sphericity of the spherical segments using a Fizeau interferometer. We show form measurement results for a full-field measuring tilted-wave interferometer and compare the form measurement results in the spherical segments with measurement results obtained with the Fizeau interferometer. © The Authors. Published by SPIE under a Creative Commons Attribution 4.0 Unported License. Distribution or reproduction of this work in whole or in part requires full attribution of the original publication, including its DOI. [DOI: [10.1117/1.OE.58.9.092602](https://doi.org/10.1117/1.OE.58.9.092602)]

Keywords: metrology; freeform; reference artifact; traceability; interferometry; measurement comparison.

Paper 181644SS received Nov. 16, 2018; accepted for publication Feb. 8, 2019; published online Mar. 26, 2019.

1 Introduction

Asphere and freeform surfaces play a central role in modern optical systems of all kinds.^{1,2} Nevertheless, accurate manufacturing is still a challenging task that depends on how well such forms can be measured. Currently, no primary reference measuring instrument with sufficiently low uncertainty of well below 50 nm exists.³ [Here and in the following, the term uncertainty refers to the expanded uncertainty ($k = 2$).⁴] Therefore, evaluating the performance of asphere and freeform measurement systems still represents a bottleneck situation in the highly accurate manufacturing of these forms.

To reliably calibrate or test the performance of such measurement systems within a short time, well-known artifacts are required in asphere and freeform metrology. Several standards for testing optical and tactile measuring machines have already been published.^{5–7} The drawback of these artifacts is that their form does not match the most common asphere and freeform lenses used in the optical industry. Simple geometries such as spheres and flats are also unsuitable because the dynamic range of asphere and freeform metrology systems cannot be tested with them in an easy manner. Since the forms of typical asphere (and freeform) surfaces are not well-known,³ these surfaces are also unsuitable for use in highly accurate calibrations of such measurement systems.

For this reason, we decided to develop artifacts whose characteristic features would be measurable via established reference measurement techniques, e.g., classical radius measurement technique or standard Fizeau interferometry. We refer to such artifacts as “metrological reference

surfaces” (MRSes).^{8,9} Typically, an MRS has a different surface form than those used in optical products. Such an MRS needs to be designed by means of a continuous surface function. Furthermore, the surface should be optically smooth and hardened to allow measurements to be performed with optical as well as tactile measuring instruments. Additionally, because the form of the MRS should be as stable as possible, thermo-invariant material is desirable. This allows the comparability of the measurement results to be improved. Ultimately, the goal of this development is to use MRSes to identify the performance of optical and tactile asphere and freeform measuring instruments. For this purpose, the characteristic features of the MRSes that will be used for the performance tests need to be calibrated with an absolute height uncertainty of well below 50 nm.

In this article, we show recent advancements in the design, manufacturing, and measurement of a so-called multispherical freeform artifact (MFA), which is one of the MRSes proposed. The first results for this special artifact have been presented previously.^{8,9} This paper is structured as follows: the design and the manufacturing process of the MFA are described in Sec. 2. In Sec. 3, the calibration of the MFA using a standard Fizeau interferometer is described. To demonstrate the purpose of the MFA, a tilted-wave interferometer (TWI) is used as an example of a freeform measuring instrument. Form measurement results of this TWI and comparisons to the calibration results are presented in Sec. 4. Finally, some conclusions are given in Sec. 5.

2 Design and Manufacturing

The MFA is a nonrotational symmetric artifact. It combines spherical segments with different radii of curvature that can be arranged in different ways. The realization we use in this

*Address all correspondence to Ines Fortmeier, E-mail: ines.fortmeier@ptb.de

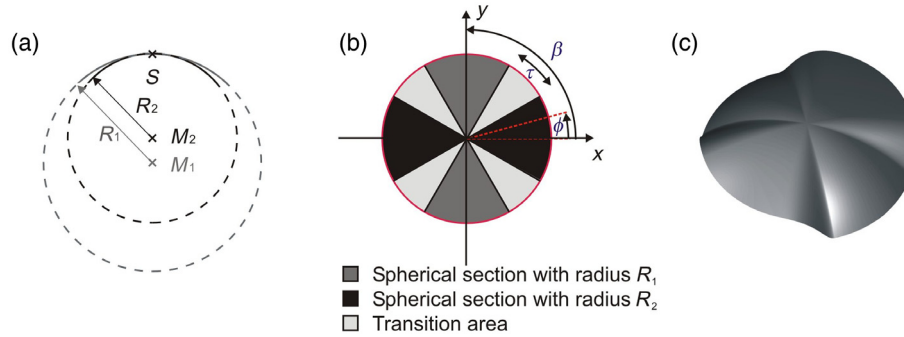


Fig. 1 Definition of the MFA: (a) the two spheres with radii R_1 and R_2 that have the same vertex S in the center. The arrangement of the spherical sections in a cylinder coordinate system is shown in (b) and a plot of the specimen height values using extreme values of R_1 and R_2 to demonstrate the shape of the artifact is shown in (c).

article is the arrangement of four spherical segments ($N = 4$) with two different radii R_1 and R_2 ; their projection onto a plane perpendicular to the axis as defined by the two sphere centers is similar to the sectors of a circle. The spherical sections have the same vertex S in the center of the specimen (see Fig. 1).⁹

Starting with a cylinder coordinate system, the transition zones between the spherical segments are defined using a cosine function, thus allowing the specimen's surface and gradient to be described by means of a continuous function. The functional design is defined as follows: the number of spherical segments is $N = 4$, the width of the transition area is called $\tau = \frac{\pi}{6}$, and the width between the middle of two adjacent spherical segments is given by $\beta = \frac{2\pi}{N} = \frac{\pi}{2}$, where $\beta > \tau$. To divide the specimen into different angular segments, the following definition is used: $\varphi = \arctan 2(x, y) + 2\pi$. With the boundary definitions $\vec{b}_1 = [\pi - (\frac{\beta+\tau}{2}), \pi - (\frac{\beta+\tau}{2}) + \beta, \pi - (\frac{\beta+\tau}{2}) + 2\beta, \dots, \pi - (\frac{\beta+\tau}{2}) + (N+1)\beta]$ and $\vec{b}_2 = [\pi - (\frac{\beta+\tau}{2}) + \tau, \pi - (\frac{\beta+\tau}{2}) + \tau + \beta, \pi - (\frac{\beta+\tau}{2}) + \tau + 2\beta, \dots, \pi - (\frac{\beta+\tau}{2}) + \tau + (N+1)\beta]$, we get the following specimen definition in a Cartesian coordinate system.

For the transition area, which is valid within the boundaries ($b_{1k} \leq \varphi < b_{2k}$, $k = 1, 2, \dots, N+1$), we get

$$z(x, y) = \sqrt{R_{tr}^2 - x^2 - y^2} - R_{tr},$$

$$\text{with } R_{tr} = \frac{R_2 - R_1}{2} \cos\left(\frac{\pi}{\tau} \left(\varphi + \frac{\tau}{2} - \frac{\beta}{2}\right)\right) + R_2 - \frac{R_2 - R_1}{2}, \quad (R_1 > R_2).$$

For the two spherical segments with radius R_1 , which are valid within the boundaries ($b_{2k} \leq \varphi < b_{1k+1}$, $k = 2, 4, \dots, N$), we get

$$z(x, y) = \sqrt{R_1^2 - x^2 - y^2} - R_1.$$

Finally, for the two spherical segments with radius R_2 , which are valid within the boundaries ($b_{2k} \leq \varphi < b_{1k+1}$, $k = 1, 3, \dots, N+1$), the following equation is valid:

$$z(x, y) = \sqrt{R_2^2 - x^2 - y^2} - R_2.$$

The diameter of the specific artifact is 40 mm. The design radii of the spherical segments of this specific artifact amount to $R_1 = 40$ mm and $R_2 = 39.5$ mm and can be absolutely

calibrated using a radius measurement bench.^{8,9} The sphericity of the four spherical segments can be calibrated using a common Fizeau interferometer, as shown in this article.

For better data comparison, we decided to add fiducial markers to the specimen. To this end, we used four Gaussian peak markers that had different depths and widths and placed them onto the four edges of the specimen by defining them as follows:

$$z_{G1}(x, y) = a_1 \cdot e^{-\frac{(x)^2 + (y-y_0)^2}{(2\sigma_1)^2}},$$

$$z_{G2}(x, y) = a_2 \cdot e^{-\frac{(x)^2 + (y-y_0)^2}{(2\sigma_2)^2}},$$

$$z_{G3}(x, y) = a_2 \cdot e^{-\frac{(x-x_0)^2 + (y)^2}{(2\sigma_2)^2}},$$

$$z_{G4}(x, y) = a_1 \cdot e^{-\frac{(x-x_0)^2 + (y)^2}{(2\sigma_1)^2}},$$

with the values $a_1 = 1 \mu\text{m}$, $a_2 = 0.5 \mu\text{m}$, $y_0 = 17$ mm, $x_0 = 17$ mm, $\sigma_1 = 0.5$ mm, and $\sigma_2 = 0.3$ mm. The different widths and depths were chosen in such a way that the data orientation was unique. This simplifies the alignment of one measurement dataset with another during data comparison. The values of the widths and depths, as well as the distance of the markers to the specimen aperture, were chosen in such a way that it was possible to measure them using optical and tactile measurement instruments.

The benefit of using Gaussian peak functions is that the markers are clearly defined by a continuous function, thus generating a smooth transition between the sample design function and the fiducials.

Thus, the complete design function is a combination of the basic specimen design and the four markers, leading to

$$z_{\text{complete}}(x, y) = z(x, y) + z_{G1}(x, y) + z_{G2}(x, y) + z_{G3}(x, y) + z_{G4}(x, y).$$

Adding the fiducials to the design is also advantageous because they can be manufactured within the same manufacturing process as the multiradii design. Initial prototypes of the MFA were manufactured using an ultraprecision diamond turning machine (Nanotech 250 UPL). For this

purpose, the artifacts were made from oxygen-free copper since copper has good machinability. The low hardness and scratch resistance were accepted for the first workpieces, which were measured only in a noncontact mode. The first measurement results of this manufacturing step, which demonstrate the manufacturability of such a specimen, had previously been published in Refs. 8 and 9. Close cooperation between the manufacturing and measurement departments allowed the manufacturing result to be optimized, especially by eliminating “overshooting” at the borders of the transition zones.

The ultraprecision lathe is capable of machining nonrotationally symmetric surfaces due to the captured angle of the spindle, which allows the angular position of the workpiece to be included in the trajectory planning of the machine. The acceleration of the axis perpendicular to the face of the workpiece is fast enough to follow the targeted rotating contour in a significant range of revolutions per minute (RPM). Ultraprecision machines usually use a constant rotation velocity of the working spindle. This is unusual for standard turning operation, as the cutting speed is not constant during a face turning process due to the changing distance from the center of rotation. In ultraprecision turning, the cutting speed may affect the surface quality to a lesser extent than the imbalance of the workpiece due to the changing rotational speed, as the chipping process is completely different to that of conventional machining.

In the first run of ultraprecision machining, the RPM was constant and high enough that the workpiece was manufactured within ~ 1 h. This is advantageous due to the low impact of thermal changes in the environment and in the machine itself. The still-relative high tangential velocity led to some overshooting of the axis that carries the tool and follows the surface at a high speed in a normal direction. High acceleration and large masses brought the system to the limits of its capability of precise positioning in the nanometer range.

In the next machining step, the cutting speed was reduced significantly, allowing the subsequent error and overshooting of the linear axis to be avoided. The chipping process of copper itself is known to be very good at very low velocities, which is known as “ruling” in ultraprecision machining. One drawback to ruling a surface with such a large area is the

increased machining time of several hours, which requires a proper thermal management system.

The MFA was measured after each manufacturing loop using the TWI, and the measurement result had been used to optimize the manufacturing parameters of the machine.

When using the TWI for characterization of the MFA, one must bear in mind that the measurement uncertainty of the TWI is expected to be well below 100 nm for this kind of specimen. However, the uncertainty evaluation of this interferometer is not yet complete; a fact that may influence the interpretation of the measurement results. In the following figures, we have named the measurement results as “deviations from the design,” which includes the measurement uncertainty of the TWI as well as the deviation from the design caused by the manufacturing process.

A comparison between a previous MFA and an optimized MFA made of copper is shown in Fig. 2.

Figure 2 shows the measured deviation from the design of a previous MFA [Fig. 2(a)]⁸ and that of an optimized MFA [Fig. 2(b)]. The peak-to-valley (PV) value is clearly reduced by a factor of at least 13, e.g., from a value of $>4 \mu\text{m}$ to 302 nm. The root-mean-square (RMS) value of the former result [Fig. 2(a)] is 502 nm⁸ and is reduced to 19 nm. This corresponds to an improvement factor of about 26. Of note is the fact that the overshooting at the transition zones between the different sections of the MFA is eliminated. It should be noted that Fig. 2(a) presents an incomplete picture of the aperture of the specimen (40 mm); the PV value at the outer aperture is even larger. With this result, much better calibration results are possible, and the artifact can be used for characterization of measurement system performance much more reliably.

In the second step, we coated the premachined copper parts with a nickel phosphorous (NiP) layer and manufactured the MFA from this material. NiP coating was chosen due to the high quality of the machined surfaces and the long operational lifespan of the tool. Electroless nickel employs chemical processes to obtain clean and pure amorphous nickel deposits with a phosphorous content of between 7% and 12%. The metal is pure enough that the average surface roughness is in the single-nanometer range and the diamond is not affected by impurities or parasitic metal or brittle contents.

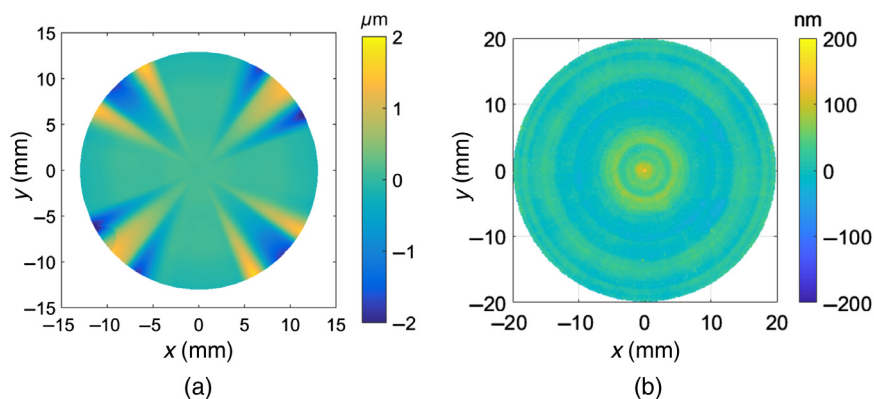


Fig. 2 Comparison between a previously manufactured MFA and an optimized MFA made of copper. The differences between the measured and the design surface forms are shown. The previous result [Fig. 2(a)] is taken from Ref. 8.

Such a coating gives the surface greater hardness, thereby allowing it to be used as a reference for low-force tactile measurement systems. Figure 6 shows the measurement result obtained after optimizing the manufacturing process for this material. For manufacturing, the cutting speed was as low as that used for manufacturing the uncoated artifact. The PV deviation of the NiP-coated artifact from the desired design form is around 200 nm, thus making it better than the previous MFA presented in the earlier article by Blobel et al.⁸ by a factor of >20. The RMS value of the measured deviation from the desired design form is 39 nm for the NiP-coated artifact, leading to an improvement factor of >13 compared to the MFA presented by Blobel et al.⁸

The PV value of the NiP-coated artifact is also slightly better than the result of the uncoated artifact [Fig. 2(b)], whereas the RMS value is slightly worse. These slight differences (within the range of a few 10-nm RMS) between the coated and uncoated artifact are assumed to be mainly caused by thermal effects during processing.

3 Calibration of the Multispherical Freeform Artifact

The MFA has two properties that can be calibrated by means of a reference technique. First, as shown by Blobel et al.,⁸ the two radii of the four spherical segments can be calibrated absolutely by means of a radius measuring bench.

In this article, we show that the sphericity in the spherical segments can also be calibrated using a standard Fizeau interferometer. For this purpose, a Zygo Verifire™ MST Fizeau interferometer with a high-quality transmission sphere is used. The transmission sphere was calibrated by means of a silicon sphere manufactured within the scope of a project on the redetermination of the Avogadro constant,¹⁰ which, in turn, was calibrated with an uncertainty of 1.4 nm ($k = 2$). When performing these measurements, care was taken to measure close to the position where the Zernike-coefficient defocus is zero and to correct the measurements to this exact condition by subtracting the defocus and appropriate spherical aberration terms.¹¹ The longitudinal (height) measurement uncertainty of this setup amounts to 11 nm ($k = 2$).

The Fizeau interferometer delivers longitudinal height values, h , for the image detector pixels, which can be represented by their relative aperture coordinates ($p, \in [-1, 1]$). These pixel coordinates correspond to horizontal and vertical angle coordinates (α_x, α_y) that result from the interferometer objective's imaging properties. With α being the objective's aperture angle, the relation

$$\alpha_x = \frac{\alpha}{2} \cdot p \quad \text{and} \quad \alpha_y = \frac{\alpha}{2} \cdot q$$

results. This angular information is transformed first into a spherical coordinate system by means of

$$\vartheta = \sqrt{\alpha_x^2 + \alpha_y^2} \quad \text{and} \quad \varphi = \tan^{-1} \frac{\alpha_x}{\alpha_y}$$

and then into a Cartesian system using the following well-known formulas:¹²

$$x = r \cdot \sin \vartheta \cdot \cos \varphi,$$

$$y = r \cdot \sin \vartheta \cdot \sin \varphi,$$

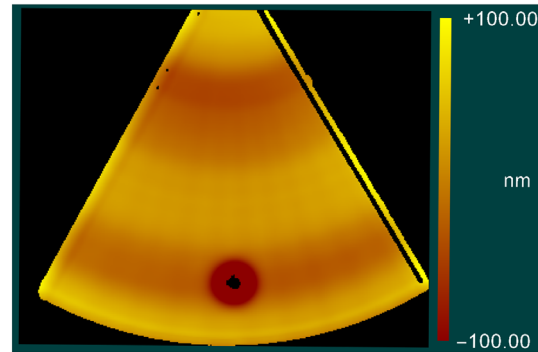


Fig. 3 Detail of the Fizeau interferometer image showing a Gaussian marker with an invalid data point in the center (black) when measuring the MFA.

$$z = r \cdot \cos \varphi.$$

Because the Fizeau interferometer measurement represents the sphericity of the specimen, the absolute radius R , which was determined in a separate measurement on a radius bench,⁸ must be added to h , and the radius coordinate r becomes

$$r = R + h.$$

In this article, we present and discuss results for the measured sphericities of the spherical segments of an MFA made of copper coated with a NiP layer. The marker structures are visible and can be used for correctly orienting the segments with respect to the design of the MFA since the different widths and depths of the marker are visible and distinguishable. It should be noted that the steep slopes of the marker structures affect the standard interferometer, resulting in the form data of the marker structures being slightly incorrect (see Fig. 3).

4 Form Measuring Results Obtained with the Tilted-Wave Interferometer and Validation

4.1 Measurement System

The TWI is a special full-field interferometric measurement device for measuring the form of aspherical and freeform surfaces.¹³⁻¹⁷ It combines a special noncommon path setup with ray tracing and model-based evaluation procedures to determine the form of such surfaces. The basic setup is shown in Fig. 4.

The illumination concept of a common interferometer is expanded using a two-dimensional (2-D) microlens array and a special pinhole mask.^{13,14} Each microlens acts as a single point-light source located in the focal plane of the interferometer collimator. Due to this 2-D arrangement, differently tilted wavefronts are generated behind the collimator and used to illuminate the surface under test (SUT).¹³⁻¹⁷ Furthermore, a beam stop in the Fourier plane of the imaging optics limits the fringe density at the detector and avoids subsampling effects.¹³⁻¹⁷ With this setup, depending on the local slope of the specimen, several small sub-interferograms ("patches") are generated at the detector. To avoid interference from the light of adjacent light sources, only every second light source in each row and column of

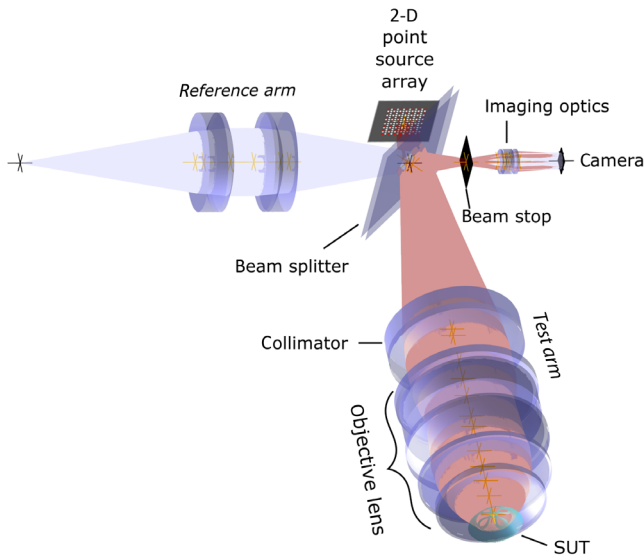


Fig. 4 Basic schematic setup of the TWI with some example rays shown passing through the system. The 2-D point source array is made up of a microlens array combined with a special pinhole mask. The light entering the microlens array and the reference arm originate from the same coherent light source (not shown).

the source array is switched on at the same time.^{13–17} Therefore, four camera images are needed to obtain the data covering the whole SUT. The number and size of the patches generated depend on the form of the SUT and on its measurement position.¹⁷ To reconstruct the form of the SUT from this data, a complex mathematical evaluation procedure is needed.^{13–17} Based on the assumption that every deviation of the SUT leads to a characteristic change in the optical path length differences (OPDs) between a source and a pixel, the measured OPDs are compared to the simulated OPDs using the design function of the SUT.^{13–17} By comparing the measured OPDs to the simulated OPDs, the form of the SUT is reconstructed by solving a nonlinear inverse problem. Since simulations of the measurements are part of the evaluation procedure, a “calibrated” model of the system is needed. To this end, the design model of the interferometer is adapted to the real system by performing measurements of known surfaces at several positions in the test space. This data are compared to simulated data; the difference is used to automatically correct the model parameters, which may be real physical model parameters or the parameters of a black-box model,^{15,16} by solving another inverse problem.

4.2 Measurement Results

The MFA is measured with the TWI. The four simulated camera images that are typical for this special freeform and for the measurement position chosen are shown in Fig. 5.

To cover the whole MFA, 39 patches are used. Initial results of the measurements of the artifacts made of copper are shown in Fig. 2. In Sec. 4.3, the artifact made of copper coated with a NiP layer is considered; this artifact has also been measured with the Fizeau interferometer. The deviation from the design surface measured by means of the TWI is shown in Fig. 6.

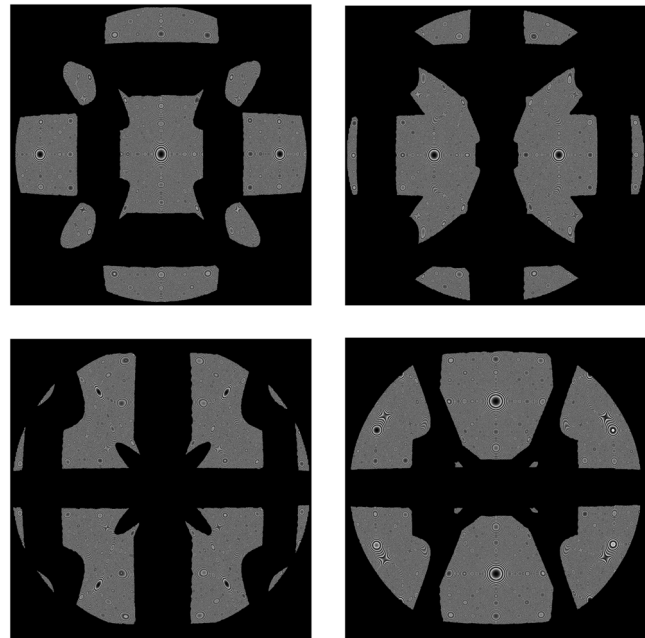


Fig. 5 Simulated camera images for the MFA with radii $R_1 = 40$ mm and $R_2 = 39.5$ mm for the TWI. The lighter areas are the 39 sub-interferograms that are used for the reconstruction of the form of the SUT. After information from the 39 patches of the four camera images has been combined, the complete aperture of the SUT can be measured. For the measurement, the nominal measurement position of the SUT was 7.359 mm away from the last surface of the objective. The position was chosen as a good compromise between the number and the size of the patches.

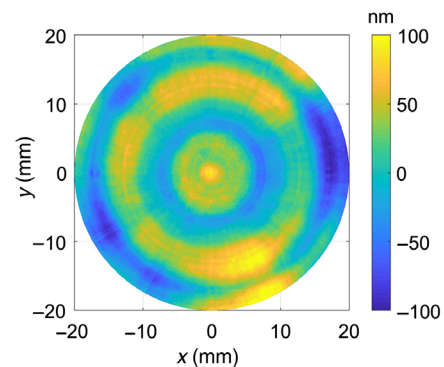


Fig. 6 Reconstructed deviations from the design of the MFA measured by means of the TWI. The artifact is made of copper coated with a NiP layer. It is remarkable that the marker structures are also nearly invisible in this difference image. This means that the design, the manufacturing result, and the measurement result agree very well.

With the TWI, the complete MFA can be measured in one procedure. The deviation from the design has a PV value of 242 nm and an RMS value of 39 nm. As a more robust parameter,¹⁸ the median-absolute deviation (MAD) is also calculated and amounts to 32 nm. As is apparent in the deviation from the design, the four Gaussian peak markers have also been manufactured and measured very well. Only slight deviations from the designs are visible in Fig. 6. Unlike the Fizeau interferometer measurements, no spherical aberration correction is necessary.

4.3 Comparison

To validate the result, the sphericities in the spherical segments are compared with the results of the standard Fizeau interferometer. To this end, the following procedure is applied.

1. Selection of the spherical segments to be evaluated (segments with either $R_1 = 40$ mm or $R_2 = 39.5$ mm)
2. Selection of a common grid of the segmented part and interpolation of the Fizeau interferometer result and the TWI result to the x , y data of the common grid.
3. Selection of the regions containing the Gaussian peak markers by identifying the areas where the z values of the design function of the markers (z_{G1} , z_{G2} , z_{G3} , and z_{G4} , see Sec. 2) are >2 nm. Thus, these are the regions, where the markers affect the overall z values z_{complete} by >2 nm. The data from these regions are hidden. This step is performed because it is not possible to measure the markers well with the Fizeau interferometer.
4. Limitation of the aperture evaluated to a value of 39.6 mm to reduce effects at the borders.

5. For the area chosen, subtraction of a best-fit sphere from both datasets since only the sphericity (i.e., the deviation from a best-fit sphere) is calibrated by the Fizeau interferometer.
6. Calculation of the pointwise difference between the two datasets obtained in step 5.

Figure 7(a) shows the sphericity of the two segments with a design radius of $R_1 = 40$ mm measured with the Fizeau interferometer, and Fig. 7(b) shows the sphericity measured with the TWI. The figures also show the RMS values of the sphericities measured, which amount to about 30 nm for the Fizeau interferometer as well as for the TWI. The MAD value amounts to only about 25 nm in both cases and shows that the artifact has been manufactured well. The pointwise difference for the two segments with a design radius of $R_1 = 40$ mm is shown in Fig. 7(c). The RMS value of the pointwise difference amounts to only 8 nm, whereas the MAD value amounts to only 6 nm.

Figure 8(a) shows the sphericity of the two segments that have the design radius $R_2 = 39.5$ mm measured with the Fizeau interferometer, and Fig. 8(b) shows the sphericity measured with the TWI. The RMS values amount to 29 nm

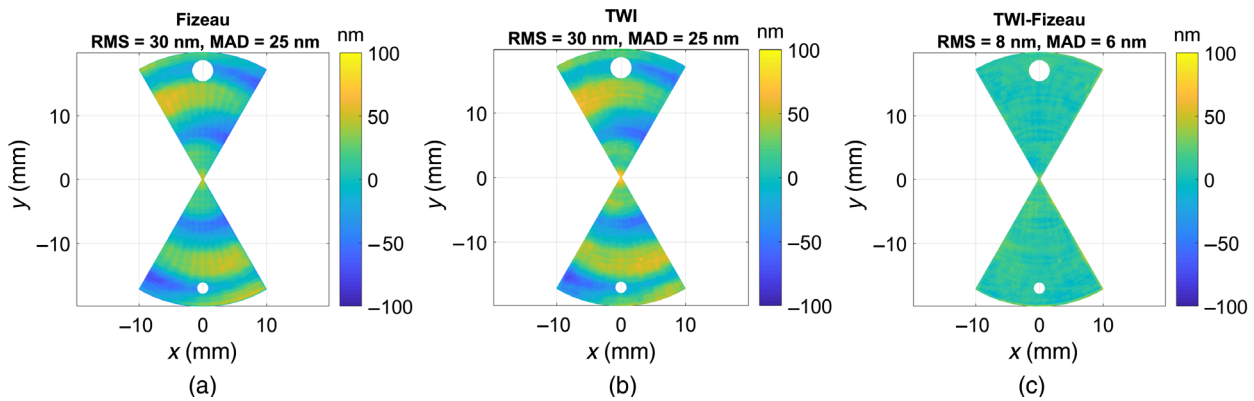


Fig. 7 (a) and (b) The measured sphericity of the MFA segments that have radius R_1 . (a) The result of the Fizeau Interferometer and (b) the result of the TWI. In (c), the pointwise difference between the result of the TWI and that of the Fizeau interferometer is shown. The Gaussian peak markers are hidden since they could not be calibrated with low uncertainty with the Fizeau interferometer.

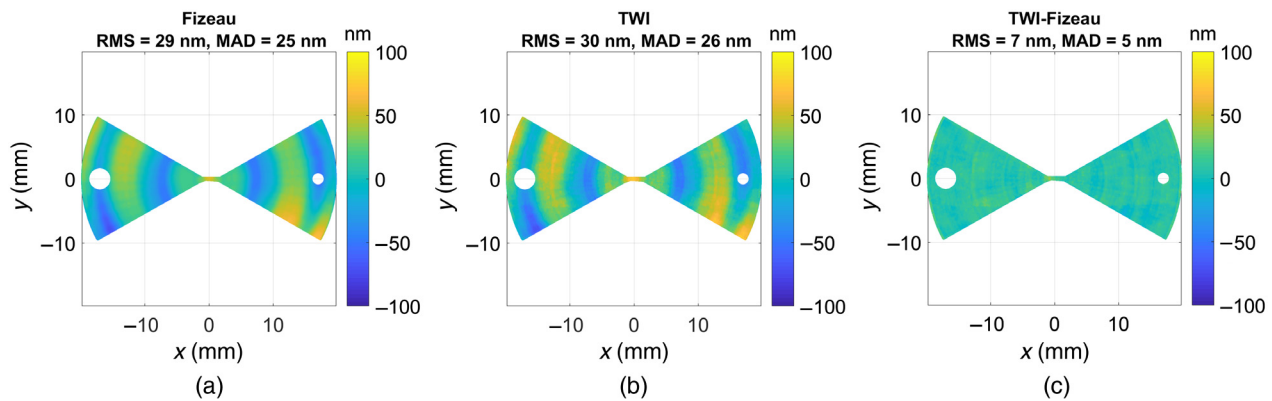


Fig. 8 (a) and (b) The measured sphericity of the MFA segments that have radius R_2 . (a) The result of the Fizeau Interferometer and (b) the result of the TWI. In (c), the pointwise difference between the result of the TWI and that of the Fizeau interferometer is shown. The Gaussian peak markers are hidden since they could not be calibrated with low uncertainty with the Fizeau interferometer.

for the Fizeau interferometer measurement and 30 nm for the result of the TWI, whereas the MAD values amount to 25 nm for the Fizeau interferometer measurement and 26 nm for the TWI measurement. The pointwise difference for the two segments with a design radius of $R_2 = 39.5$ mm is shown in Fig. 8(c). The RMS value of the pointwise difference amounts to only 7 nm and the MAD value is 5 nm. Thus, these values are very close to the values of the other two segments with the larger radius.

These results and values show that the measurement result of the TWI is very close to the result of the reference measurement of the Fizeau interferometer, leading to the conclusion that the TWI can measure the sphericities in the spherical sections of this freeform very well.

5 Conclusions

MRSes have characteristic features that are measurable with a traceable reference measurement technique. The special MFA has two properties—the radii of their spherical segments and their sphericities—that can be calibrated by means of traceable reference measurement techniques.

In this article, we have presented a significant improvement in the manufacturing process; this improvement is the result of a very closed-loop optimization process between manufacturing and measuring. The difference (RMS value) between the form of the manufactured artifact and its design form was reduced by a factor of >20 compared with the MFA manufactured without this optimization process (e.g., from a value much >500 nm to about 20 nm). Furthermore, we coated the MFA with NiP to ensure that it could also be used as a reference artifact for low-force tactile measurement systems. Additionally, four Gaussian peak fiducial marker structures were added to the design to improve the comparison with results obtained by means of other measurement techniques.

The procedure presented here to manufacture the MFAs and to calibrate their radii and (most importantly) sphericities is a promising approach to producing a traceable reference standard that can be used to validate asphere and freeform measurement instruments. By way of example, we have shown the measurement result of the TWI. The agreement of the sphericity in the spherical segments with the result of the Fizeau interferometer is remarkably good and has an RMS error of about 8 nm, which is comparable to the height measurement uncertainty of the Fizeau interferometer. Furthermore, the steep slopes at the marker structures were measured and manufactured successfully since they are almost invisible in the measured deviation from the design.

Within the scope of an active European project (EMPIR 15SIB01),¹⁹ the MFA will be developed from a thermo-invariant material such as super invar to increase the form stability of this artifact. In this project, the uncertainty of the radius measurement will also be reduced to 100 nm ($k = 2$)⁴ for complete spherical sections. The radius measurement uncertainty that can be achieved by the proposed techniques for the (incomplete) spherical sections of the MFA discussed here will be investigated in future work. Assuming an uncertainty of the radius measurements for this MFA of about 200 nm ($k = 2$), a height uncertainty

estimation resulted in an overall uncertainty of about 30 nm ($k = 2$). This fulfills the requirement mentioned in Sec. 1 concerning the traceability and uncertainty of a calibration device.

In the future, the radii of the optimized MFA will also be calibrated and compared to the radii obtained by asphere and freeform measurement instruments.

To enlarge the field of application, the manufacturability of the MFA with other radii or reflectivity has to be investigated in future.

Acknowledgments

The authors sincerely thank the EMPIR organization. The EMPIR is jointly funded by the EMPIR participating countries within EURAMET and the European Union (15SIB01: FreeFORM). The authors also thank Manuel Stavridis of PTB's Data Analysis and Measurement Uncertainty working group for his technical support. The authors declare that there are no conflicts of interest.

References

1. G. Schulz, "Aspheric surfaces," Chapter IV in *Progress in Optics*, E. Wolf, Ed., North-Holland Physics Publishing, Amsterdam, pp. 349–415 (1988).
2. B. Braunecker, R. Hentschel, and H. J. Tiziani, *Advanced Optics Using Aspherical Elements*, SPIE Press, Bellingham, Washington, pp. 292–307 (2008).
3. R. Schachtschneider et al., "Interlaboratory comparison of aspheres," *Meas. Sci. Technol.* **29**, 055010 (2018).
4. Joint Committee for Guides in Metrology, "Evaluation of measurement data—guide to the expression of uncertainty in measurement," JCGM 100:2008, BIPM Joint Committee for Guides in Metrology, Paris (2008).
5. B. Acko et al., "Standards for testing freeform measurement capability of optical and tactile coordinate measuring machines," *Meas. Sci. Technol.* **23**, 094013 (2012).
6. S. Robson et al., "Artefacts for optical surface measurement," *Proc. SPIE* **8085**, 80850C (2011).
7. M. McCarthy et al., "NPL freeform artefact for verification of non-contact measuring systems," *Proc. SPIE* **7864**, 78640K (2011).
8. G. Blobel et al., "Metrological multispherical freeform artifact," *Opt. Eng.* **55**, 071202 (2016).
9. M. Schulz et al., "Concept of metrological reference surfaces for asphere and freeform metrology," in *EUSPEN's 17th Int. Conf. and Exhib.*, Hannover (2017).
10. A. Nicolaus et al., "Volume determination of two spheres of the new ²⁸Si crystal of PTB," *Metrologia* **54**, 512–515 (2017).
11. P. de Groot, T. Dresel, and B. Truax, "Axial alignment for high-precision interferometric measurements of steeply-curved spheres," *Surf. Topogr. Metrol. Prop.* **3**, 044004 (2015).
12. I. N. Bronstein et al., *Taschenbuch der Mathematik*, 5th ed., p. 218, Verlag Harri Deutsch, Frankfurt (2001).
13. E. Garbusi and W. Osten, "Perturbation methods in optics: application to the interferometric measurement of surfaces," *J. Opt. Soc. Am. A* **26**, 2538–2549 (2009).
14. E. Garbusi, C. Pruss, and W. Osten, "Interferometer for precise and flexible asphere testing," *Opt. Lett.* **33**, 2973–2975 (2008).
15. G. Baer et al., "Calibration of a non-null test interferometer for the measurement of aspheres and free-form surfaces," *Opt. Express* **22**, 31200–31211 (2014).
16. I. Fortmeier et al., "Analytical Jacobian and its application to tilted-wave interferometry," *Opt. Express* **22**, 21313–21325 (2014).
17. I. Fortmeier et al., "Evaluation of absolute form measurements using a tilted-wave interferometer," *Opt. Express* **24**, 3393–3404 (2016).
18. P. J. Huber, "Robust statistics," in *International Encyclopedia of Statistical Science*, M. Lovric, Ed., Springer, Berlin, Heidelberg, pp. 1248–1251 (2011).
19. EMPIR, "FreeFORM project," EMPIR 15SIB01, 2016–2019, <https://projects.ptb.de/emrp/freeform-home.html>.

Biographies of the authors are not available.